Available online at www.sciencedirect.com
ScienceDirect
Journal of Power Sources 162 (2006) 262–270
JOURNAL OF POWER SOURCES
www.elsevier.com/locate/jpowsour

Characterization of the operational parameters of a H_2/air micro PEMFC with different flow fields by impedance spectroscopy☆

Shou-Shing Hsieh*, Sheng-Huang Yang, Chih-Lun Feng

Department of Mechanical and Electro Mechanical Engineering, National Sun Yat-Sen University, Kaohsiung, Taiwan, ROC

Received 25 May 2006; received in revised form 21 June 2006; accepted 21 June 2006
Available online 1 August 2006

Abstract

The operational parameters of a H_2/air micro proton exchange membrane fuel cell (PEMFC) with different flow configurations (mesh, serpentine, and interdigitated) were investigated by impedance spectroscopy. The operational parameters include the cell operating temperature and the anode backpressure. The above parameters affected the high frequency straight line as well as the medium frequency and low frequency arcs. The influence in terms of impedance on the dynamic response of the present H_2/air micro fuel cell under different operating conditions and flow geometry were quantitatively measured, which it allows insight into the nature of these effects and consequently a better understanding of the micro PEM fuel cell system that could be helpful for the design and operation of the fuel cell.

Keywords: Micro PEMFC; EIS; Operational parameters; SU-8 flow field plates

1. Introduction

Hydrogen/air proton exchange membrane (PEM) fuel cells are highly attractive as power sources for mobile applications and portable electronic devices, since they operate at a relatively low temperature (e.g., 60 °C) with high power densities. However, the performance in terms of voltage/current density (*V*/*I*) curves and power/current density (*P*/*I*) curves of low temperature fuel cells, such as PEM fuel cells, needs substantial improvement. For instance, at low current density, the activation overpotential is large, and at high a current density, other problems are generated, such as transport limitation of O_2 to the catalyst sites. In addition, the reactant gas flow field design could also limit the performance of the PEM fuel cell. The performance of PEM fuel cells is known to be influenced by many parameters, such as the operating temperature, the pressure, and the feed rate of the gas streams [1–3]. To improve fuel cell performance, it is necessary to understand these parametric effects, including the flow geometry.

Modeling electrochemical systems (e.g., a fuel cell) by an equivalent circuit is a procedure used in the electrochemical impedance spectroscopy (EIS) technique that determines the influence of each component on fuel cell performance. The EIS provides data on fuel cell system macroscopic and microscopic properties. It was long recognized that EIS is a useful and powerful technique to study the different processes that occur in the fuel cell [4]. It seems, however, that limited data are available in the open literature for the dynamic response of micro fuel cells under different operating conditions and flow field geometries.

As a typical component of a PEMFC, a plate etched with grooves serves as gas supply channels, two such plates sandwiching a layer of membrane electrode assembly (MEA) on their grooved side comprise a single PEMFC. H_2 is fed to the channels on the anode side, and similarly, air is fed to the channels on the cathode side. These provide the gas flow and heat removal [5]. There are two flow streams of anode gas and cathode gas to be considered in a PEMFC. When electrochemical reactions take place, the reactant gases (H_2/air) in both streams experience substantial variations in concentration and mass flow. Consequently, the flow field, temperature and reactant species concentration distributions in both channels significantly influence the cell performance. Therefore, the flow channel geometry plays an extremely important role.

☆ Part of this work was presented at 4th International Conference on Fuel Cell Science, Engineering and Technology, Irvine, Californian, June 19–21, 2006.

* Corresponding author. Tel.: +886 7 5252000x4215; fax: +886 7 5254215.
E-mail address: sshsieh@mail.nsysu.edu.tw (S.-S. Hsieh).

0378-7753/$ – see front matter © 2006 Elsevier B.V. All rights reserved.
doi:10.1016/j.jpowsour.2006.06.070

The PEMFC has many advantages compared with other types of fuel cell as a portable power source. The application of fuel cells in portable powering is motivated by demands of 3C (communication, computing, and camcorder) products [6,7] and is challenged by several factors. For instance, a high power density and high energy-to-weight ratio [8]. Miniaturizing fuel cells for portable applications is not simply a matter of reducing the corresponding component dimensions. Rather, new design and manufacturing processes must be examined and developed simultaneously. In addition, operating parameters as well as flow field configurations during operation should be optimised.

The electrochemical measurements of the present micro PEMFCs exhibit a complex impedance curve due to a GDL/metal interaction of carbon paper and silver electrode. Such reaction mechanisms involve a series of kinetic parameters. Generally, these kinetic parameters can be obtained by fitting the impedance spectrum to the equivalent circuit. In general, one or two semi-circular arcs may be found. Based on the literature, the partial pressure of O_2 and cell operating temperature would affect the magnitude of the polarization resistance, R_P. This is because the O_2 reaction mechanism involves a reduction on the GDL/metal of carbon cloth and silver, followed by diffusion of O_2 through the mixed conductor towards the MEA (i.e., the electrolyte). In fact, a strong correlation has been observed between the electrode kinetics and the surface exchange of O_2 and the bulk O_2 diffusion. The present micro PEMFCs' design and structure would have similar kinetics. In addition, due to large differences in morphology of the electrode and Pt loading MEA, and test conditions, i.e., temperatures and O_2 partial pressure, different rate determining steps would occur for O_2 reduction [9].

In this study, electrochemical impedance spectroscopy measurements were carried out to get *in situ* information on the effect of the three different flow field patterns; namely, mesh, serpentine, and interdigitated, types, as well as the operational parameters such as cell temperature and backpressure at the anode in the operation of a micro PEMFC.

2. Experimental

A single PEM fuel cell with an active surface area of 2.25 cm × 2.25 cm was used for all experiments in this study. The membrane electrode assembly (MEA) consisted of a Nafion 112 membrane in combination with a platinum loading (Lyntech) of 1 and 0.5 mg cm^{-2} on cathode and anode, respectively. Two 290 μm carbon papers (ELAT) served as the gas diffusion layers (GDLs) and were added to the MEA.

2.1. Flow field plate and construction of a micro PEMFC

Besides the above-stated MEAs preparation, microfabrication of the flow field plate using deep UV lithography was performed. SU-8 (MicroChem, Newton, MA) materials were chosen for prototyping the complex geometric structures for the flow path. Electrically conducting regions acted as the current collectors and were patterned onto the surface by sputtering silver to a thickness about 200 nm. Three different types of flow patterns were made, i.e., mesh, serpentine, and interdigitated. The detailed geometry and size of the channels used are listed in Table 1. A LIGA-like microfabrication process of deep UV lithography with SU-8 thick photoresist material was used to fabricate the microchannels for the flow fields. It is described below and illustrated in Fig. 1. More information can be found in ref. [10].

Table 1
Operating parameter and flow field configuration

	Cell temperature		
	25 °C	35 °C	50 °C
Backpressure			
Anode	97 kPa	153 kPa	207 kPa
Cathode	Forced air		
SU-8 flow field channel ($H \times W \times L$)			
Mesh	200 μm × 500 μm × 22.5 mm		
Interdigitated	200 μm × 2000 μm × 22.5 mm		
Serpentine	200 μm × 250 μm × 22.5 mm		
MEAs			
Nafion 112	Anode: Pt on Carbon (0.5 mg cm^{-2}) Cathode: Pt on Carbon (1 mg cm^{-2})		
GDL	Anode: carbon cloth based material Cathode: carbon cloth based material		
Electrode	Silver (anode/cathode): 200 nm × 22.5 mm × 22.5 mm		

1. The substrate, a 50 μm-thick Cu film was cleaned with acetone for 3 min and heated to 150 °C for 3 min.
2. Spin coating of SU-8 to a thickness 200 μm was carried out; different rotating speeds (500 rpm for 120 s, 1000 rpm for 60 s, and 500 rpm again for 5 s) were applied to the Cu substrate.
3. Soft baking for about 35 min was applied (50 °C for 5 min, 90 °C for another 5 min, and, finally, 95 °C for 25 min).
4. Ultraviolet light with a wavelength at 350 nm was used for the exposure process; SU-8 was lithographically structured simultaneously.
5. Once exposure was completed, heat was applied again for a post-exposure bake of about 8 min.
6. Development was done with an ultrasonic wave oscillator for a microstructured channel (200 μm depth, 200 μm width with a 50 μm rib).
7. Ag film (0.2 μm) was sputtered onto the top of the ribs between the channels and lateral sidewalls as well as bottom floor of the channels.

Fig. 2(a and b) show the fuel cell test fixture, which includes deep UV lithography SU-8 flow fields with different flow patterns (mesh, serpentine, and interdigitated), providing a 5 cm^2 single cell geometry. The sandwiched layered (2 flow field plates + 2 carbon papers + MEAs) structure was finally pressed onto a 2 mm polymethylmethacrylate (PMMA) gasket (housing) as shown in Fig. 3. The entire assembly was bound using UV curing, one of the surface mount technologies (SMT).

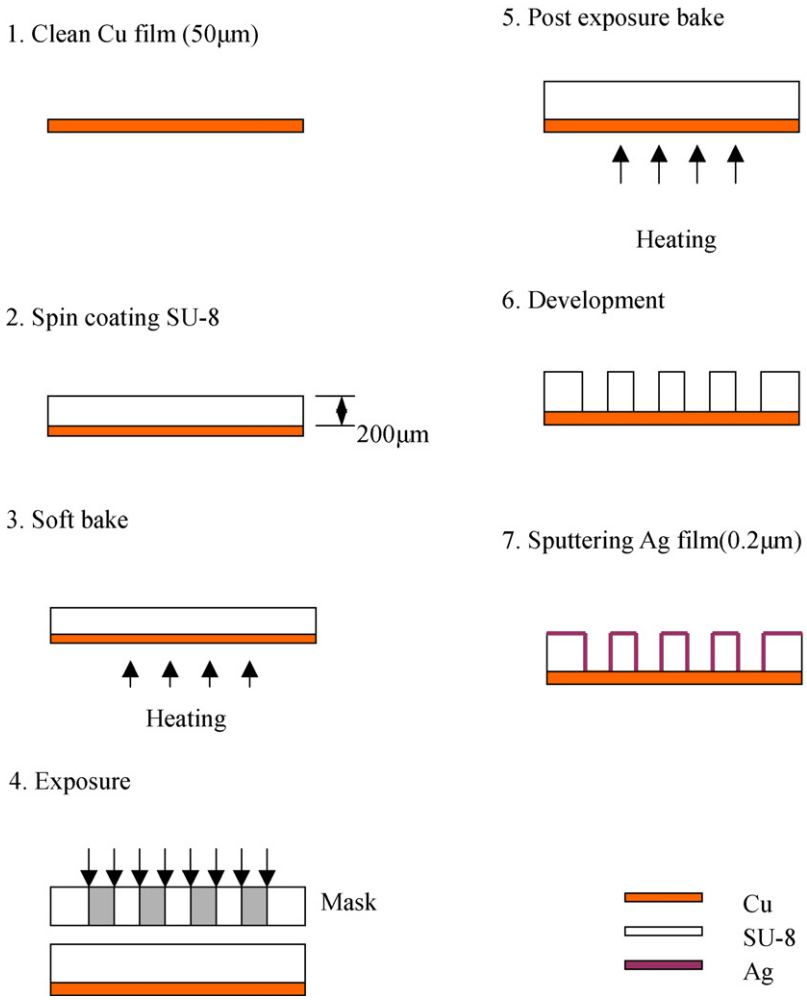

Fig. 1. Fabrication processes of flow field plates.

2.2. Operating conditions and EIS

In our experiments, the mass flow rates of hydrogen and air were kept at 10 sccm and the fuel cells were operated at cell temperatures of 25, 35, and 50 °C with pressures in the anode compartment of 97, 153, and 207 kPa, respectively. The EIS technique was used to reveal what causes the performance difference among the operational parameters change such as cell operating temperatures and backpressures at the anode, and three different flow field patterns. The excitation amplitude of the ac signal was 10 mV rms and the frequency was typically varied from 0.1 Hz to 100 kHz. A Gamry PC 4/750 potentiostat and Gamry electrochemistry software Version 4.35 were used to conduct the measurements. The performance of PEM single cells was evaluated in an in-house test station under the control of mass flow, temperature, and pressure. The impedance spectra were measured in the steady state. The reproducibility of the impedance spectra was ±2.5% by magnitude and ±1.5% by phase angle. The fitting of the impedance spectra to the transfer function derived on the basis of a kinetic model was performed by using software. The standard error of estimate of the kinetic parameters calculated by the above-stated procedure was within ±3.5%. The present experiments were performed in a clean room at the University Microsystem Research Laboratory with ambient air relative humidity of 40%.

3. Results and discussion

Prior to the cell bonding, the Pt loading MEAs were examined by SEM to observe the morphological conditions of the surface coverage of the MEAs (not shown).

3.1. V/I and P/I curves

The electrode–electrolyte assemblies were investigated in a single cell test station. Steady state performance was achieved by operating the fuel cell with pure hydrogen and air feed. Polarization and power density curves results obtained at 50 °C and a backpressure of 153 kPa in the presence of H_2 and air feed with mesh, serpentine, and interdigitated flow patterns on the anode and the cathode are shown in Fig. 4. The cell was fully activated even in a dry condition.

In all the experiments, the interdigitated flow field showed better performance than the other two types. For example, the single cell *V/I* curves in Fig. 4 show a better performance for the interdigitated channel designs as compared to the mesh and

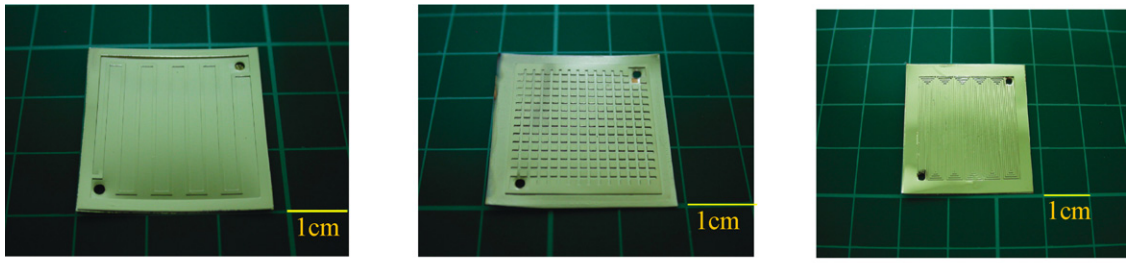

interdigitated flow field mesh flow field serpentine flow field

(a)

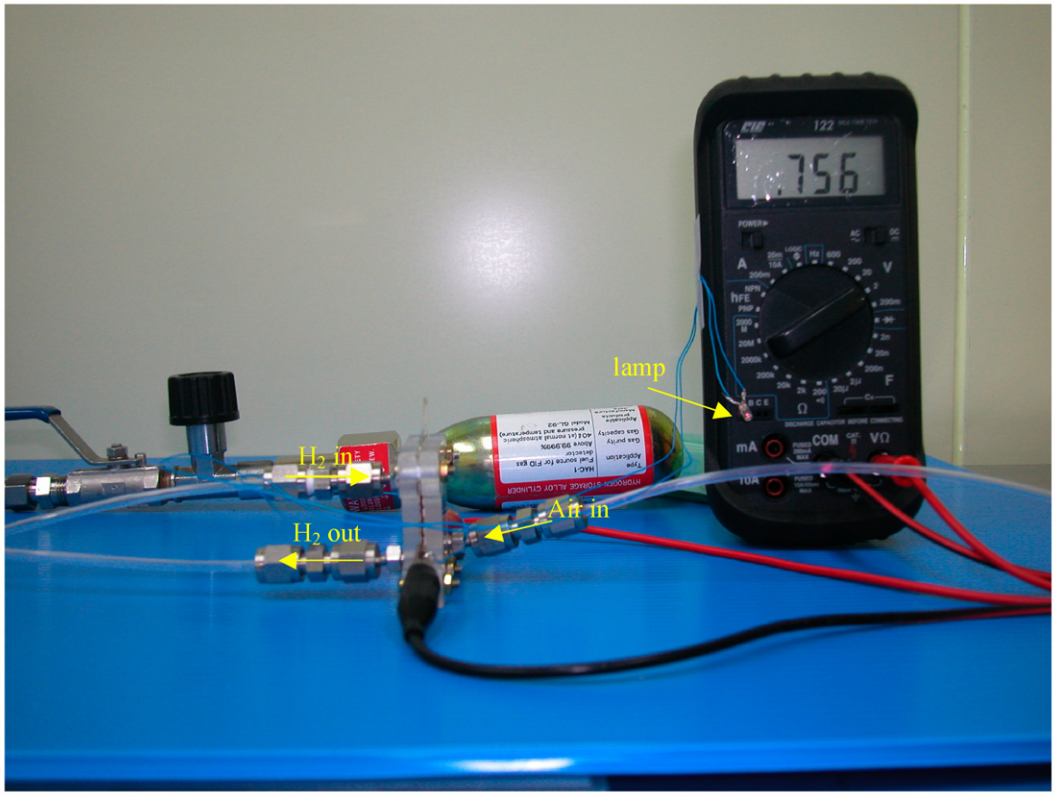

(b)

Fig. 2. Flow channel configurations and single fuel cell at operating condition: (a) the configurations of three flow channel and (b) interdigitated flow channel for single fuel cell.

serpentine flow patterns. This is because the convective flow promoted by the interdigitated flow fields allows a higher utilization of the Pt catalyst. The *V*/*I* curves have an initial rapid voltage drop at a very small current range due to the electrochemical activation process, which is caused by the sluggish kinetics of O_2 reduction at cathode [1]. Thus, the ohmic polarization controls the remaining part of curves, in which the voltage decreases linearly with increasing current density [2]. Furthermore, considerable deviations from linearity were observed at a high current density indicating the existence of mass transfer limitations. The corresponding *P*/*I* curves are shown in Fig. 5 and again strongly indicate that the interdigitated flow patterns show performance superiority. In addition, the performance of the present H_2/air micro PEMFC is improved with increase of operating pressure and cell temperature (not shown), in good agreement with previous studies of traditional PEMFCs [1–3].

3.2. Electrochemical analysis

Using EIS, it is possible to study the electrocatalytic properties of the fuel cell by analyzing the impedance of a full cell with the different operating backpressures and temperatures and three different flow field plates. With the impedance of full cell (anode side: H_2; cathode side: air) measured, the impedance spectra reveal information about both the anode impedance and the cathode impedance. The impedance spectrum of a full cell equals nearly the cathode impedance because the H_2 oxidation reaction is fast [9]. Based on the above, two or three depressed arcs in the spectrum were observed. To explain this, the equiv-

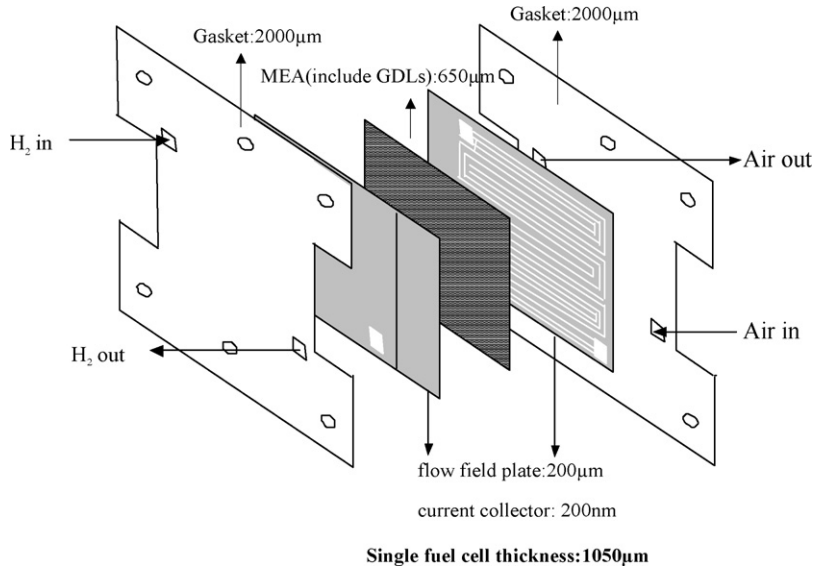

Fig. 3. The construction of micro fuel cell.

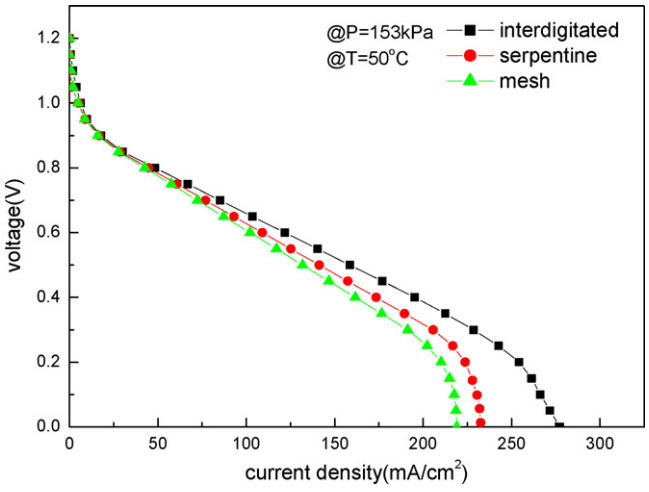

Fig. 4. *V*/*I* curve of three configurations channel at $P = 153$ kPa and $T = 50\,^{\circ}$C.

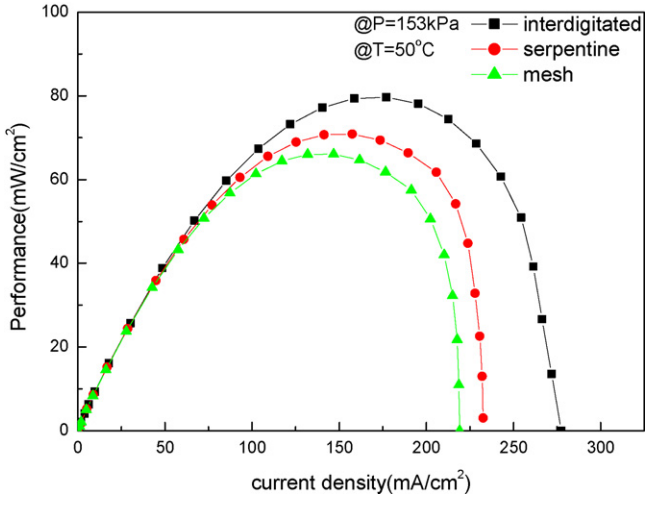

Fig. 5. *P*/*I* curve of three configurations channel at $P = 153$ kPa and $T = 50\,^{\circ}$C.

alent circuit [12] can be applied and is shown in the inset of each figure where L is an inductance and R_Ω represents the electrolyte resistance, and R_{ct} and R_d stand for the high frequency arc, medium frequency arc, and low frequency arc resistances, depending on each case. To describe the depressed arc, the well-known CPE (constant phase element) is used. The CPE is defined by

$$Z_C = \frac{1}{Z_0(j\omega)^n} \tag{1}$$

where $j = (-1)^{1/2}$, ω the angular frequency, Z_0 a dimensional constant, and n is the exponent constant and may vary between -1 and 1. If $n = 1$, CPE is ideal capacitance and $Z_0 = C_{dl}$. When $n = 0.5$, CPE is Warburg impedance. If $n = 0$, CPE is ideal resistance, and if $n = -1$, CPE is inductance. The depressed arc means that this electrode system is non-homogenous and leads to a distribution of time constants in limited regions [11]. Furthermore, introducing $n > 1$ accounts for the fact that at high frequency the ac current does not entirely penetrate the pores. The depth of this penetration decreases as ω increases, which causes the pore surface area involved to decrease. At low frequency, the entire surface is involved (i.e., $n \to 1$) and again the CPE is represents a pure capacitance. Generally, a considerable separation in frequencies between the kinetic semicircle and the 45° diffusion region is observed for the three different flow channel configurations. The equivalent circuits used in this model can be denoted as shown in Table 2, where R_Ω is the membrane resistance and Q stands for the CPE. Detailed kinetic parameters can be obtained by fitting the spectrum to the equivalent circuit. In fact, CPE analysis can characterize the role of Q to be either a capacitance, resistance, or inductance. The fitted Nyquist diagrams nearly coincide with the measured ones as shown in Figs. 6–11 to within ±3.5% as stated previously and the calculated parameters and deviations for each case are listed in Table 2.

Table 2
Kinetic parameters from regression

	I (H)	R_Ω (Ω)	C_{dl}	n_1	R_{ct} (Ω)	C_d	n_2	R_d (Ω)	Error (%)
Interdigitated									
97 kPa									
25 °C	1.8516×10^{-6}	0.299	46.524×10^{-3} S^{n_1}	0.509	3.622	10^{-3} S^{n_2}	0.967	0.497	2.612
153 kPa									
25 °C	1.653×10^{-6}	0.297	48.652×10^{-3} S^{n_1}	0.519	3.292	10^{-3} S^{n_2}	0.967	0.485	2.372
35 °C	1.778×10^{-6}	0.389	49.612×10^{-3} S^{n_1}	0.589	2.874	10^{-3} S^{n_2}	0.973	0.412	2.517
50 °C	1.731×10^{-6}	0.411	74.286×10^{-3} S^{n_1}	0.573	1.903	10^{-3} S^{n_2}	0.963	0.297	2.891
207 kPa									
25 °C	1.746×10^{-6}	0.298	58.373×10^{-3} S^{n_1}	0.591	2.212	10^{-3} S^{n_2}	0.941	0.347	2.774
	I (H)	R_Ω (Ω)	C_{dl}	n_1	R_{ct} (Ω)	C_d	n_2	R_d (Ω)	Error (%)
Mesh									
97 kPa									
25 °C	1.689×10^{-6}	0.297	6.187×10^{-3} S^{n_1}	0.575	3.994	0.789 S^{n_2}	0.814	1.258	2.891
153 kPa									
25 °C	1.657×10^{-6}	0.296	5.787×10^{-3} S^{n_1}	0.601	3.647	0.589 S^{n_2}	0.911	1.031	3.473
35 °C	1.841×10^{-6}	0.321	2.811×10^{-3} S^{n_1}	0.589	3.214	0.617 S^{n_2}	0.864	0.774	3.037
50 °C	1.713×10^{-6}	0.381	3.411×10^{-3} S^{n_1}	0.617	2.793	0.783 S^{n_2}	0.854	0.643	2.743
207 kPa									
25 °C	1.662×10^{-6}	0.308	5.537×10^{-2} S^{n_1}	0.617	3.073	0.541 S^{n_2}	0.971	0.822	2.977
	I (H)	R_Ω (Ω)	C_{dl}	n_1	R_{ct} (Ω)	C_d	n_2	R_d (Ω)	Error (%)
Serpentine									
97 kPa									
25 °C	1.741×10^{-6}	0.291	13.316×10^{-3} S^{n_1}	0.487	3.491	10^{-3} S^{n_2}	0.983	0.817	2.047
153 kPa									
25 °C	1.632×10^{-6}	0.292	14.871×10^{-3} S^{n_1}	0.521	3.214	10^{-3} S^{n_2}	0.982	0.714	2.214
35 °C	1.685×10^{-6}	0.375	36.825×10^{-3} S^{n_1}	0.582	2.981	10^{-3} S^{n_2}	0.971	0.603	2.853
50 °C	1.687×10^{-6}	0.432	4.122×10^{-3} S^{n_1}	0.622	2.531	0.824 S^{n_2}	0.973	0.621	3.012
207 kPa									
25 °C	1.578×10^{-6}	0.291	12.716×10^{-3} S^{n_1}	0.523	2.794	10^{-3} S^{n_2}	0.989	0.452	2.633

Equivalent circuit

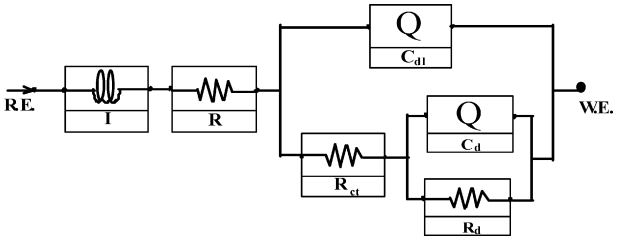

R_{ct} is the charge transfer resistance for the O_2 at the electrode surface, which corresponds to the diameter of the semicircle in the medium and the low frequency domain of the impedance plots in the present study. The Warburg impedance consists of a series combination of a capacitance (C_d) and a diffusion resistance (R_d) due to the reaction sites. Since the dispersion effects exist for the present electrochemical system, the constant phase element, CPE, also denoted as Q, which corresponds to the double layer capacitance at the electrode/gas/catalyst interface, was used instead of an ideal capacitor in the study in order to minimize errors from non-linear regression. Generally, a capacitive loop can be cited for the relation of the surface coverage of intermediate species, which reduces the overall reaction rate.

3.2.1. Effect of anode backpressure

Although one may argue that the EIS of a H_2/air PEMFC at different anode backpressures cannot give accurate kinetic information due to variation in the compression of the cell and an uneven pressure distribution on both electrodes, in the present study it is possible to examine such effects on the micro fuel cell.

Nyquist plots obtained by the impedance for cells operated at 0.7 V are shown in Figs. 6–8, at 25 °C with different flow channels and three backpressures. One or two semi-circular loops corresponding to oxygen reduction exist. An equivalent circuit can fit the characteristics of an electrochemical interface by a non-linear regression least square method. The equivalent circuit used to represent this data involves a resistance R_Ω in series with the circuits shown in the inset of Figs. 6–8, where R_{ct} is the

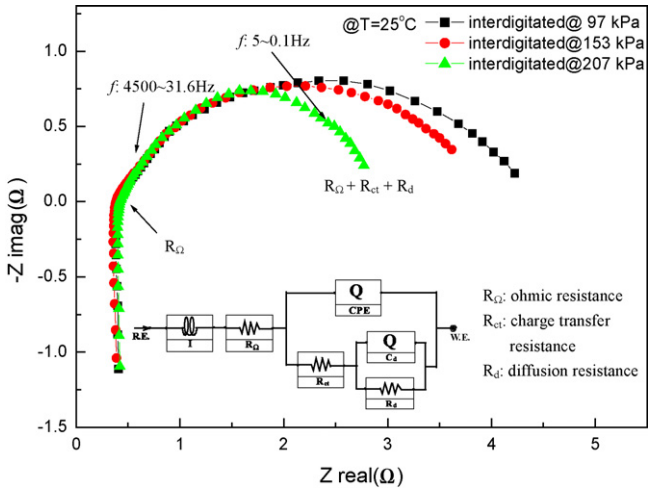

Fig. 6. Impedance spectra of full cell at three operating pressures for interdigitated flow field.

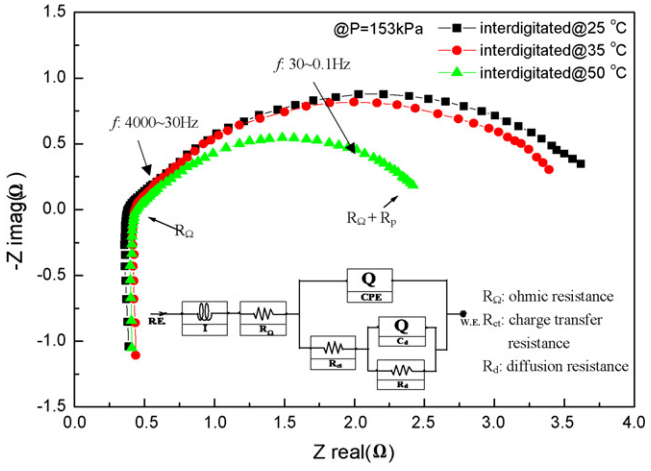

Fig. 9. Impedance spectra of full cell at three operating temperatures for interdigitated flow field.

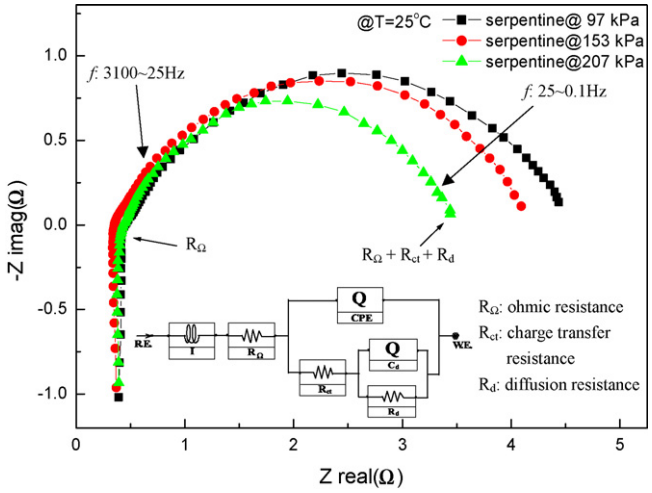

Fig. 7. Impedance spectra of full cell at three operating pressures for serpentine flow field.

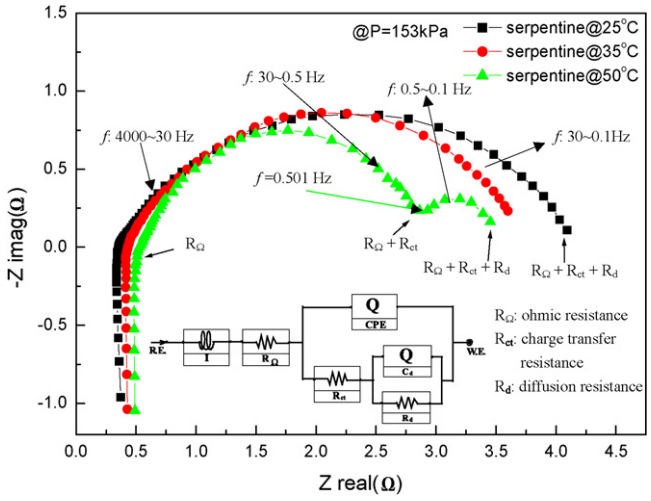

Fig. 10. Impedance spectra of full cell at three operating temperatures for serpentine flow field.

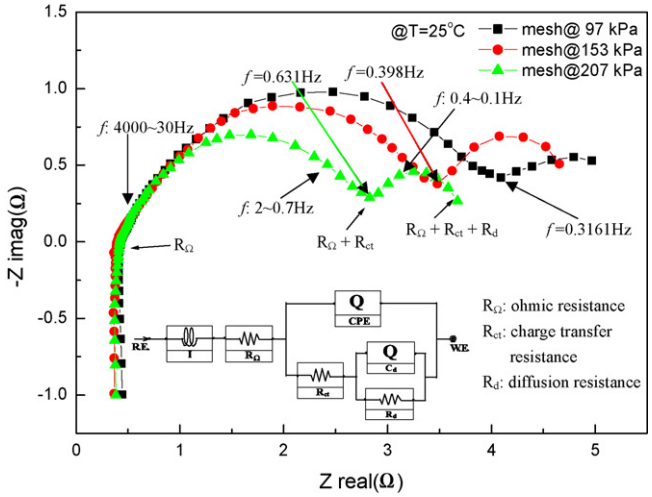

Fig. 8. Impedance spectra of full cell function of operating pressure for mesh flow field.

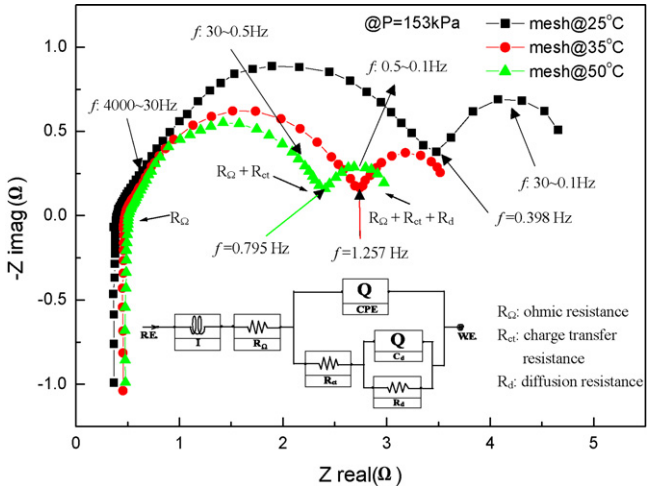

Fig. 11. Impedance spectra of full cell at three operating temperatures for mesh flow field.

charge transfer resistance, C_d the diffusion capacity, R_Ω represents the electrolyte resistance, R_d the diffusion resistance due to the gas crossing through the GDL and catalytic layer, and C_{dl} is the electrochemical double layer capacity, morphological properties of the electrode and adsorption phenomena. This double layer forms in part due to diffusion effects and also because of the reactions between the electrons in the electrodes and the ions in the electrolyte. Table 2 reports the values for R_Ω (membrane resistance), R_{ct}, C_{dl}, n_1, R_d, C_d, and n_2 calculated from the fit of these data for each case.

Generally speaking, the ohmic resistance R_Ω for each cell is relatively constant but slightly increases as the cell temperatures increase. The polarization resistance is the sum of the charge transfer resistance (R_{ct}) and diffusion resistance (R_d). It can be seen in Fig. 6 that there are two distinct areas: one high frequency straight line (≅4.5 kHz) and one medium (≅1 Hz) frequency arc. The inductance I (≅1.48–1.75 μH) is caused by the lead wire and is seen at the highest frequencies. The high frequency straight line representing the charge transfer resistance R_{ct} seems slightly to decrease while the anode backpressure increases. This 45° straight line corresponding to $n_1 \cong 0.55$ (0.51–0.59) in Eq. (1) indicates the purely diffusional Warburg element. Only the medium frequency arc seems to be closed as a loop and the diameter of this semi-circle represents the sum of the charge transfer resistance R_{ct} across the catalyst and electrolytes as well as the diffusion resistance R_d on the electrode interfaces. This also reflects the electrochemically active surface area of the electrode for the adsorption/desorption processes of hydrogen and oxygen on Pt at its interface with Nafion. In general, capacitive loops represent the relaxation of surface coverage of intermediate species which reduce the overall reaction rate in the transient regime. The reduction in R_{ct} (3.29–2.21 Ω) with the increase of the backpressure can be explained in terms of increase of ionic conductivity and extension of the gas/electrolyte/electrode interface. An increase in R_{ct} is also indicative of an increase in the gas/catalyst/electrode interface resistance which is insufficient to provide an adequate electrolytic conductivity inside the catalyst layer, resulting in a low Pt utilization and a high ohmic drop. Similar results were also obtained in Fig. 7 for the serpentine flow pattern. However, the values of R_{ct} (3.49–2.79 Ω) are larger due to a poor Pt utilization in the serpentine flow configuration as compared to that of the interdigitated flow field.

Unlike interdigitated and serpentine flow channels, the mesh flow channel shows two semi-circle loops as shown in Fig. 8 where both the medium frequency arc and the low frequency arc seem to be a loop, and they were detected as a hump at different frequency f (∼0.316–0.631 Hz) and the size seemed to grow as the anode backpressure increased. The complex impedance spectra were mainly caused by water formation/accumulation in the channel-type electrode structures adjacent to the present three flow field configurations. Furthermore, such situations would be dominant in a mesh flow field. Consequently, two semi-circular loops (medium and low frequency) were formed in EIS plots. Similarly, it is clear that the charge transfer resistance decreases with increasing backpressure. In addition, among the three flow patterns, it is apparent that the interdigitated flow field has the least ohmic drop as evident from the sum of the charge transfer resistance (R_{ct}) and the diffusion resistance (R_d) (≅2.56–3.78 Ω). Generally speaking, for the three cases studied herein, it is found that the impedance decreased with operating pressure increase. Furthermore, at $P = 207$ kPa, it seemed to have a larger effect on the EIS as compared to those at $P = 97$ and 153 kPa.

3.2.2. Effect of cell operating temperature

The effect of the cell operating temperature on the EIS spectra can be seen in Figs. 9–11 at an anode backpressure of 153 kPa for each flow field. The complex impedance spectrum is very similar to those of Figs. 6–8 as expected because it can be extracted from either one of Figs. 6–8. Among these operating temperatures, for each channel at 50 °C as shown in Figs. 9–11, one can obtain the least resistance [13]. The charge transfer resistances were found for the interdigitated channel at about 3.29, 2.87, and 1.90 Ω, respectively, for the corresponding cell temperatures of 25, 35, and 50 °C in Fig. 9. Again, an inductance at a higher frequency was found. Overall, the charge transfer resistance decreases with an increasing cell operating temperature caused by an increase in the diffusional component with membrane dehydration, which is also in agreement with ref. [12]. In addition, the decreased rate of charge transfer resistance seems different for three cell temperatures. Unlike Fig. 7, Fig. 10 does show a second capacitance loop (a hump was detected at $f = 0.501$ Hz) at a cell operating temperature 50 °C for the serpentine flow field, which strongly suggests that the cell temperature has a bigger influence than that of the anode backpressure.

3.2.3. Effect of flow field configuration

Generally, different flow fields would compress different regions of the MEA to different extents causing variations in the ionic resistance in the catalyst layers and the membranes. This compression would also affect the porosity of the catalyst and GDL to different extents and influence transport processes and electronic resistance as well.

As stated previously, the present study covers three different flow channels; namely, mesh, serpentine, and interdigitated flow patterns. Based on the previous figures shown, one can conclude that the interdigitated channel has the least charge transfer resistance as well as the diffusion resistance (R_d) in comparison to the other two flow patterns. This is because the increase in cell performance (i.e., the least R_{ct} and R_d) in the interdigitated pattern is directly related to the convective effect on the transport mechanism, shown by the absence of medium or low frequency arc or semicircle, which increases the amount of reagent that reaches the so called three phase zone where the reactions takes place. Meanwhile, and most importantly, the convective flow assists removal of any liquid water formed or accumulated in the channel-type electrode structure, whose presence forces the H_2/air into a two phase transport medium. However, such beneficial effects are less evident in the mesh flow pattern, where the transport is by diffusion, and in the serpentine, where diffusion predominates [14].

In addition, water accumulation retards the electron transfer at the electrode surface and so reduces the electron transfer rate. The main characteristic feature of the curves measured on the

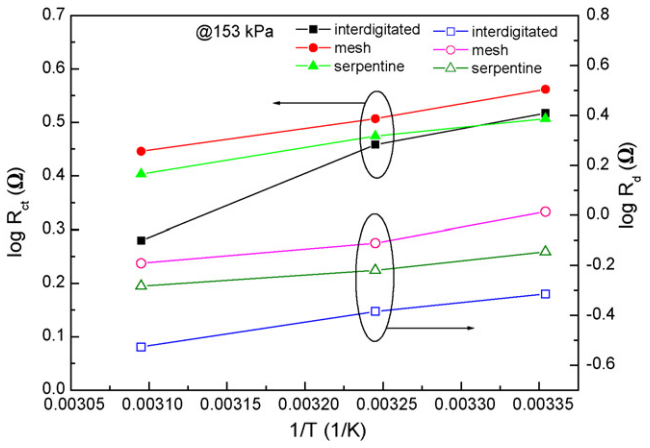

Fig. 12. Charge transfer resistances and diffusion resistances vs. cell operating temperature.

electrode interface (Ag/Pt) appear to be a "passivating" behavior of the water vapor against the O_2 adsorption. Again, from Table 2, we can see that the electron transfer resistance (R_{ct}) for the mesh flow channel electrode can be 1.2 times higher than that for interdigitated flow channel. The increase in n_1 and n_2 from about 0.5 to about unity for all the cases studied reflects the change in the surface electrode process from Warburg diffusion to a capacitive behavior. However, the variations of values of n_1 and n_2 seem not significant for the different flow channel configurations. Finally, in Fig. 12, the logarithm of R_{ct} and R_d are plotted against $1/T$ at $P = 153$ kPa in which the effect of the flow field pattern and cell operating temperature can be further analysed. The crossover in Fig. 12 is due to the high and low temperature effects on charge transfer R_{ct} between the mesh and serpentine flow patterns. However, the resistance is consistently low in the present study for interdigitated flow configurations.

4. Conclusions

The effect of the anode gas backpressure, cell operating temperature, and the flow field configuration of a H_2/air micro PEMFC was examined by ac impedance spectroscopy. It was found that the impedance spectra of the full cell consisted of two or three arcs. Both the charge transfer resistance and the diffusion resistance across the Pt/Ag interface (the high frequency arc) and O_2 adsorption (medium frequency arc) decreased due to water formation on the cathode with increasing anode backpressure as well as cell temperature with a decrease in the charge transfer reaction and a change in O_2 adsorption. In addition, the gas diffusion arc (the low frequency arc) was not found for interdigitated flow channels. While for mesh channel, the low frequency arc does exist, possibly due to water formation and accumulation in the gas passages. The present EIS study for a range of operating parameters of backpressure and cell temperature on different flow configurations is in good agreement with those results from the *V*/*I* and *P*/*I* curves. The effect of the operating pressure, cell performance, and flow field patterns on the impedance spectra were clearly observed.

References

[1] D. Chu, R. Jiang, J. Power Sources 80 (1999) 226–234.
[2] J.J. Hwang, H.S. Hwang, J. Power Sources 114 (2002) 24–32.
[3] L. Wang, A. Husar, T. Zhou, H. Lin, J. Hydrogen Energy 28 (2003) 1263–1272.
[4] A.G. Hombrados, L. González, M.A. Rubio, W. Agila, E. Villanueva, D. Guinea, E. Chinarro, B. Moreno, J.R. Jurado, J. Power Sources 10 (2005) 25–31.
[5] P.W. Li, L. Schaefer, Q.M. Wang, T. Zhang, M.K. Chyu, J. Power Sources 115 (2003) 90–100.
[6] J.P. Meyers, H.L. Maynard, J. Power Sources 109 (2002) 76–88.
[7] H. Chang, J.R. Kim, J.H. Cho, H.K. Kim, K.H. Chai, Solid State Ionics 148 (2002) 601–606.
[8] K.H. Choi, D.H. Peck, C.E. Kim, D.R. Shin, T.H. Lee, J. Power Sources 86 (2002) 197–201.
[9] A. Ringuedé, J. Fouletier, Solid State Ionics 139 (2001) 167–177.
[10] S.S. Hsieh, J.K. Kuo, S.H. Yang, C.F. Huang, H.H. Tsai, Energy Convers. Manage. 47 (2006) 1868–1878.
[11] M. Ciureanu, S.D. Mikhailenko, S. Kaliaguine, Catal. Today 82 (2003) 195–206.
[12] J.D. Kim, Y.I. Park, K. Kobayashi, M. Nagai, M. Kunimatsu, Solid State Ionics 140 (2001) 313–325.
[13] S.S. Hsieh, C.F. Huang, J. Kun Kuo, H.H. Tsai, S.H. Yang, J. Solid State Electrochem. 9 (2005) 121–131.
[14] A. de Souza, E.R. Gonzalez, J. Solid State Electrochem. 7 (2003) 651–657.